Numerical Experiment of Combined Infrared and Ultraviolet Radiation Remote Sensing to Determine the Profile and Total Content of Atmospheric Ozone

Cheng Minghu (程明虎), *Shi Guangyu* (石广玉)
Institute of Atmospheric Physics, Academia Sinica, Beijing 100011
and *Zhou Xiuji* (周秀骥)
Academy of Meteorological Science, State Meteorological Administration, Beijing 100081
Received November 6, 1989

ABSTRACT

A new remote sensing method is described to determine the vertical distribution and total content of atmospheric ozone. The method combines surface infrared, satellite infrared and ultraviolet channels. The width of the infrared channels is 0.01 cm^{-1}, less than Lorentz half-width at the earth's surface, rather than the present width, because these channels can obtain information about variations in the ozone profile below the profile main-peak. The numerical experiments show that the method has a satisfactory precision in determining total ozone content, just about 1 percent error, and vertical distribution from the earth to 65 km space. In addition, some semi-analysis functions for calculating backscattered ultraviolet and a relaxation equation are described in this paper.

I. INTRODUCTION

Ozone possesses a strong absorption band in the ultraviolet below about 0.3 μm, which protects the biological cycle on the earth and heats the middle-upper layer of the atmosphere. Also it is the chief constituent participating in its photochemistry (Houghton et al., 1984). Therefore ozone sounding attracts people's attention more and more.

The knowledge about ozone has a history of about 200 years (London and Angell). During this period, a series of ozone sounding techniques have been developed, and remote sensing is one of them. At present, the following remote sensing techniques are in use: Satellite infrared (Prabhukara et al., 1970), Umkehr, backscattered ultraviolet (BU) and limb technique (London et al., 1980). Techniques of microwave (Randeyger) and laser are being studied. Beside the laser technique (in fact, aerosol effects the precision seriously), these remote sensing techniques cannot precisely sound the ozone under the main-peak of the profile. To overcome the difficulty above, we describe a new remote sensing method, combining ground infrared, satellite infrared and ultraviolet techniques, to determine ozone profile and content.

II. SELECTION OF INFRARED CHANNELS

Remote sensing of ozone using its infrared emission band at 9.6 μm has been made using data from the infrared interferometer spectrometer (IRIS) instrument on Nimbus 4. Because of the very large number of closely spaced lines in this band and the ozone vertical profile, very limited ozone profile variation can be obtained using this kind of channel. Sekihara and Walshaw (1969), Shafrin (1970) and Prabhakara et al. (1970) have shown that the radiances

in different regions of the band do not actually contain much information about the ozone profile. Prabhakara et al. have shown that a statistical, one–parameter approach, which makes use of climatological data on ozone distribution, enables crude but useful approximate ozone profiles to be extracted.

In this section we investigate the narrow channels. The width of these channels is 0.01 cm^{-1}, less than the Lorentz half–width of ozone absorbing line at the earth surface. These channel spectrometers on satellite can obtain information about variations in the different ozone layers, because half–width of ozone absorbing line has a positive relation with the atmospheric pressure (McClatchey et al., 1973).

1. *Theory*

The atmosphere is considered as plane–parallel and local thermodynamic equilibrium in the 9.6 μm band. Therefore, the equation of radiative transfer can be written as (Zhou et al, 1982; Zeng, 1974)

$$\mu\frac{dI_v(z,\theta)}{d\tau_v(z)} = -I_v(z,\theta) + B_v(z) \tag{1}$$

where I_v represents the radiative intensity at wave number v, z is the height above surface, μ is cosine of zenith angle θ, B_v denotes Planck function and $\tau_v(z)$ is optical depth

$$\tau_v(z) = \int_{z_0}^{z} k_v \rho dz \tag{2}$$

where ρ and k_v are density and coefficient of absorption gases.

There are three absorption bands, O_3, H_2O and CO_2, in the 9.6 μm band. Neglecting CO_2 absorption, for it is very weak, we have

$$k_v\rho = k_{vO_3}\rho_{O_3} + k_{vH_2O}\rho_{H_2O} \tag{3}$$

Suppose that the wave number width of the radiometer is v_0 to $v_0 + \delta v$ and the responsive function of instrument is

$$\psi_m(v) = \begin{cases} 1 & v_0 < v < v_0 + \delta v \\ 0 & \text{otherwise} \end{cases} \tag{4}$$

Because the sun's radiation can be neglected and the earth's surface can be considered as black body inside the band, we obtain radiation intensity from the following equation (Cheng, 1985)

$$I_m(\theta) = \begin{cases} -\int_0^{\infty} B_m[T(z')]\frac{\partial T_m(z',0,\theta)}{\partial z'}dz' & \text{ground} \\ B_m[T(0)]T_m(\infty,0,\theta) + \int_0^{\infty} B_m[T(z')]\frac{\partial T_m(\infty,z',\theta)}{\partial z'}dz' & \text{satellite} \end{cases} \tag{5}$$

where

$$T_m(z,z_0,\theta) = \int_{\delta v} T_v(z,z_0,\theta)\psi_m(v)dv \tag{6}$$

$$T_v(z,z_0,\theta) = \exp\left(-\int_{z_0}^{z}\frac{\rho k_v}{\mu}dz\right) \tag{7}$$

$$B_m(T) = B_{v_0 + 0.5\delta v}(T) \tag{8}$$

$$B_v(T) = \frac{2hc^2 v^3}{\exp(-hvc/kT) - 1} \tag{9}$$

where T_v and T_m are the transmission functions of monochromatic v and band δv respectively; h and k are Planck and Boltzman constants; c and T are light speed in vacuum and absolute temperature respectively.

Using the method of the best information layer (Zeng, 1974) and acting variation in equation 5, we have (Cheng, 1985)

$$\delta I_m(\theta) = \int_0^\infty K_m(z, \rho_{O_3}(z), \theta) \frac{\delta \rho_{O_3}(z)}{\rho_{O_3}(z)} dz \tag{10}$$

where $K_m(z, \rho_{O_3}(z), \theta)$ is weighting function. For ground remote sensing

$$K_m(z, \rho_{O_3}(z), \theta) = \int_{\delta v} \frac{\psi_m(v)}{\mu} \int_0^z \frac{\partial B_m[T(z')]}{\partial z'} T_v(\infty, z', \theta) dz' k_{vO_3}(z) \rho_{O_3}(z) dv \tag{11}$$

and for satellite remote sounding

$$K_m(z, \rho_{O_3}(z), \theta) = \int_{\delta v} \frac{\psi_m(v)}{\mu} \{B_m[T(0)] T_v(\infty, 0, \theta) - \int_z^\infty \frac{\partial B_m[T(z')]}{\partial z'} T_v(z', 0, \theta) dz' \} k_{vO_3}(z) \rho_{O_3}(z) dv \tag{12}$$

To obtain the radiation intensity and weighting function, we use line by line method (Cheng, 1985).to calculate the absorption coefficient of ozone and water vapour using following equations:

$$k_v = \sum_{i=1}^{N} k_{iv} \tag{13}$$

$$k_{iv} = \begin{cases} \dfrac{S_i}{\pi} \dfrac{\alpha_{li}}{\alpha_{li}^2 + (v_{0i} - v)^2} & \text{Lorentz} - \text{shape} \\ \dfrac{k_{0i} y_i}{\pi} \displaystyle\int_{-\infty}^{\infty} \frac{\exp(-t^2)}{y_i^2 + (x_i - t)^2} dt & \text{Voigt} - \text{shape} \end{cases} \tag{14}$$

$$\alpha_l = \alpha_{l0} \left(\frac{P}{P_0}\right) \left(\frac{T_0}{T}\right)^n \tag{15}$$

$$S = S_0 \frac{Q_v(T_0) Q_R(T_0)}{Q_v(T) Q_R(T)} \exp(1.439 \frac{T - T_0}{T T_0} E_0) \tag{16}$$

$$Q_R = \left(\frac{T}{T_0}\right)^j \tag{17}$$

$$x = \frac{v - v_0}{\alpha_D} \tag{18}$$

$$y = \frac{\alpha_l}{\alpha_D} \tag{19}$$

$$k_0 = \frac{S}{\sqrt{\pi}}\alpha_D \tag{20}$$

$$\alpha_D = 4.301\sqrt{\frac{T}{M}}v_0 \tag{21}$$

where N is total number of absorbing lines contributing their absorption at v. α_l and α_D are Lorentz and Doppler half-width respectively. Q_V and Q_R are vibrational and rotational partition functions. Q_v and j are shown by McClatchey et al. (1973). S, v_0 and E_0 are the intensity per absorbing molecule, the resonant frequency and the energy of the lower state respectively. P is the pressure. Constants P_0, T_0 and n are taken to be standard atmospheric pressure, 296K and $1/2$. M is molecular mass. v_0, S_0, E_0 and α_{l0} are obtained from AFGL tape, 1980.

2. *Selection of the Channels*

Provided that a wave number interval δ_v is used as a remote sensing channel, as we have known, two cases will occur:

· The radiation within δv is not absorbed by the constituent at a certain altitude, the variation of the constituent at the altitude cannot be sounded by the channel. And the constituent at the altitude will not interfere with the sounding of the constituent at other altitude.

· The radiation within δv is absorbed by the constituent at a certain altitude, the variation of the constituent at the altitude can be sounded by the channel. And the constituent at the altitude will interfere with the sounding of the constituent at other altitude.

There are many absorption lines in the 9.6 μm band of ozone. When the present channel is used as remote sensing, the latter will occur for the whole atmosphere, because the channel width is larger than the half-width of absorption line and the interval between absorption lines. Therefore limited information on the variation of the ozone profile can be obtained using these channels.

According to the knowledge of the spectrum, we know that the half-width of absorption lines is very narrow and they usually do not overlap in the middle-upper atmosphere. When the channel with narrow width, such as 0.01 cm^{-1}, is used in a satellite sounding instrument, many "peaks" and "alleys" are observed. When the central numbers of channels and "peak" do not overlap, the former and the latter will occur for middle-upper and lower atmosphere respectively. Using these channels with different central wave numbers shown in Figure 1, we can determine a set of channels to sound the lower ozone profile. For ground remote sensing, absorption lines overlap due to large Lorentz half-width and lots of lines. Therefore, the method of selection channels is the same as that of the present channel.

Dividing the atmosphere into 65 layers with an interval of 1 km and using standard atmosphere (McClatchey et al., 1972) and the tape of AFGL, 1980, we calculate the weighting functions of 0.01 cm^{-1} width with different relative position to the resonant frequency of absorption lines. The variation weighting functions shown in the Figure 2 and Figure 3 are selected for remote sensing of satellite and ground respectively. The left wave numbers of the satellite channels are 1052.5098, 1052.8723 and 1052.4797 cm^{-1}, corresponding to the latitudes of the maxima of the weighting functions at 12, 18, and 20 km for satellite sounding.

3. *Discussion*

(1) *The effect of water vapour*

Figure 4 shows two variation weighting functions, central number 1052.5 cm^{-1} and width of 0.01 cm^{-1}, with and without water vapour absorption. The two curves nearly overlap and the maximum value of their difference is 0.1%. Therefore the water vapour absorption can be ignored in the practical calculation.

(2) *The weighting functions of channels with a width of* 5 cm^{-1}

Figure 5 shows two weighting functiong of channels with the width of 5 cm^{-1}, located at 967.0–972.0 cm^{-1} and 1052.0–1057.0 cm^{-1}. The latitudes corresponding to their maximum weighting functions are 20 and 24 km, respectively. Actually all peaks of weighting functions concentrate between 20 and 24 km, because the intervals of 967.0–972.0 cm^{-1} and 1052.0–1057.0 cm^{-1} are located at the wing and the peak of the 9.6 μm band. In addition, the channel of 967.0–972.0 cm^{-1} cannot give the information on variations of the ozone profile due to the very small amplitude of its weighting function. Therefore, only one independent channel, with width of 5 cm^{-1}, can be obtained in 9.6 μm band. The conclusion is the same as the former researchers'.

III. SELECTION OF BU CHANNELS

Much work has been done on sounding the vertical distribution of ozone using BU method (Aruga and Lgarashi, 1976; Heath et al., 1973; 1978). In this section, we discuss the selection of the channels and describe some semi-analytical formulas of the intensity and weighting function of BU.

1. *Theory*

In the region of 2500–3100 A, the heat radiation of the earth-atmosphere system can be neglected and the atmosphere can be considered as plane-parallel, so the radiative transfer equation can be written as:

$$\mu \frac{dI(\tau, \Omega)}{d\tau} = I(\tau,\Omega) - J(\tau,\Omega) \tag{22}$$

where $J(\tau, \Omega)$ is the source function and satisfies the equation below

$$J(\tau,\Omega) = \frac{F_0}{4} P(\Omega, -\Omega_0, \tau)\exp(-\frac{\tau}{\mu}) + \frac{1}{4\pi}\int_{4\pi} I(\tau,\Omega')P(\Omega,\Omega')d\Omega' \tag{23}$$

where P is the phase function, F_0 is the solar radiative flux.

Considering the ozone absorption and molecule scattering (Aruga and Lgarashi, 1976), we have the following equations

$$P(\Omega,\Omega',\tau)=\frac{\sigma_{ms}\rho\sum}{\sigma_{ms}\rho\sum+\rho_{O_3}k_{O_3}}r(\Omega,\Omega') \tag{24}$$

$$r((\Omega,\Omega')=\frac{3}{4}(1+\cos^2\Theta) \tag{25}$$

$$\cos^2\Theta=\sin\theta\sin\theta'\cos(\varphi-\varphi')+\cos\theta\cos\theta' \tag{26}$$

$$\sigma_{ms}=\frac{32\pi^3}{3N_e\lambda^4}(n_r-1)^2 \tag{27}$$

$$n_r-1=(16432.8+\frac{2949.81}{146-\lambda^2}+\frac{25.540}{41-\lambda^4})10^{-8} \tag{28}$$

$$\tau(z)=\int_z^\infty[\rho\sum(z')\sigma_{ms}(z')+\rho_{O_3}(z')k_{O_3}(z')]dz' \tag{29}$$

where σ_{ms} and k_{O_3} represent atmospheric molecule scattering and ozone absorption coefficients respectively. $\rho\Sigma$ and ρ_{O_3} are atmospheric molecule and ozone density. n_r is air refraction index. Ne equals $2.68719\times10^{10}\text{cm}^{-1}$. λ is solar radiation wavelength whose unit is micrometer.

Ignoring the earth surface reflection, using the successive scattering (Liou,1980) and considering up to the second scattering, we can obtain the radiative intensity for satellite review (Cheng, 1985)

The first radiative intensity

$$I_{m1}(\Omega,\Omega_0)=\frac{F_0\sigma_{ms}}{4\mu}\int_0^\infty\rho\sum(z')\exp(-\frac{\mu_0+\mu}{\mu_0\mu}\tau')dz'r(\Omega,-\Omega_0) \tag{30}$$

The second radiative intensity

$$\begin{aligned}I_{m2}(\Omega,\Omega_0)=\frac{F_0\sigma_{ms}^2}{16\pi\mu}\int_0^\infty\rho\sum(z)\int_0^1\frac{A\mu(\mu')}{\mu'}\Big[\int_0^z\rho\sum(z')\exp(-\frac{\mu_0+\mu'}{\mu_0\mu'}\tau')dz'\exp(\frac{\mu-\mu'}{\mu\mu'}\tau)\\+\int_z^\infty\rho\sum(z')\exp(\frac{\mu_0-\mu'}{\mu_0\mu'}\tau')dz'\exp(-\frac{\mu+\mu'}{\mu\mu'}\tau)\Big]d\mu'dz\end{aligned} \tag{31}$$

The total radiative intensity

$$I_m(\Omega,\Omega_0)=I_{m1}(\Omega,\Omega_0)+I_{m2}(\Omega,\Omega_0) \tag{32}$$

where

$$\begin{aligned}Au(\mu')=\frac{\pi}{16}\{&0.25[2\cos^2(\varphi-\varphi_0)+1]\sin^2\theta\sin^2\theta_0(1-\mu'^2)^2+[\cos^2\theta\sin^2\theta_0\\&+\cos^2\theta_0\sin^2\theta-2\sin^2\theta\sin^2\theta_0\cos(\varphi-\varphi_0)](1-\mu'^2)\mu'^2\\&+(\sin^2\theta+\sin^2\theta_0)(1-\mu'^2)+2[\cos^2\theta\cos^2\theta_0\mu'^4\\&+(\cos^2\theta+\cos^2\theta_0)\mu'^2+1]\}\end{aligned} \tag{33}$$

Acting variation in the equation 32, we have

$$\delta I_m(\Omega,\Omega_0)=\int_0^\infty K_m(z'',\rho_{O_3}(z''),\Omega,\Omega_0)\frac{\delta\rho_{O_3}(z'')}{\rho_{O_3}(z'')}dz''$$
$$=\delta I_{m1}(\Omega,\Omega_0)+\delta I_{m2}(\Omega,\Omega_0)$$
$$=\int_0^\infty [K_{m1}(z'',\rho_{O_3}(z''),\Omega,\Omega_0+K_{m2}(z'',\rho_{O_3}(z''),\Omega,\Omega_0)]\frac{\delta\rho_{O_3}(z'')}{\rho_{O_3}(z'')}dz'' \quad (34)$$

where

$$K_m(z'',\rho_{O_3}(z''),\Omega,\Omega_0)=K_{m1}(z'',\rho_{O_3}(z''),\Omega,\Omega_0)+K_{m2}(z'',\rho_{O_3}(z''),\Omega,\Omega_0) \quad (35)$$

$$K_{m1}(z',\rho_{O_3}(z''),\Omega,\Omega_0)=-\frac{\mu_0+\mu}{4\mu_0\mu^2}F_0 k_{O_3}(z'')\rho_{O_3}(z'')\sigma_{ms}r(\Omega,-\Omega_0)$$
$$\times\int_0^{z''}\rho\sum(z')\mathrm{Exp}(-\frac{\mu_0+\mu}{\mu_0\mu}\tau')dz' \quad (36)$$

$$K_{m2}(z'',\rho_{O_3}(z''),\Omega,\Omega_0)=\frac{F_0}{16\pi\mu}k_{O_3}(z'')\rho_{O_3}(z'')\sigma_{ms}^2\int_0^1\frac{Au(\mu')}{\mu'}$$
$$\times\{\int_0^{z''}\rho\sum(z')[(A+B)\exp(B\tau)\int_0^z\rho\sum(z')\exp(A\tau')dz'+(C+D)\exp(D\tau)$$
$$\times\int_z^\infty\rho\sum(z')\exp(C\tau')dz']dz+A\int_{z''}^\infty\rho\sum(z')\exp(B\tau')dz'\int_0^{z''}\rho\sum(z')\exp(A\tau)dz$$
$$-C\int_z^\infty\rho\sum(z')\exp(C\tau')dz'\int_0^{z''}\rho\sum(z)\exp(D\tau)dz\}d\mu' \quad (37)$$

$$A=-\frac{\mu_0+\mu'}{\mu_0\mu'} \quad (38)$$

$$B=\frac{\mu-\mu'}{\mu\mu'} \quad (39)$$

$$C=\frac{\mu_0-\mu'}{\mu_0\mu'} \quad (40)$$

$$D=-\frac{\mu+\mu'}{\mu\mu'} \quad (41)$$

2. *Selection of the BU Channel*

Using the above equations and approximate calculation (Cheng, 1985), which can save a lot of computer time, we choose 13 channels for BU remote sensing. Figure 6 shows their variation weighting functions, in which the wavelengths are 2500, 2700, 2800, 2900, 2922, 2950, 2970, 3002, 3023, 3034, 3075, and 3096 A respectively, and other parameters are $\varphi=0$, $\varphi_0=0$, and $\theta=\theta_0=30^o$.

Figure 6 shows that the peaks of these weighting functions are distributed between 23 km and 52 km. Therefore, these channels can sound the vertical distribution of ozone from 23 to 65 km. Comparing with work of Aruga et al, there are 5 additional channels taken into account. These channels cannot sound more parameters, but can reduce the random error.

IV. INVERSION OF OZONE PROFILE AND CONTENT

18 channels are employed in our combined inversion of ozone profile and content. Their weighting functions are shown in Figure 2, Figure 3, and Figure 6. The maxima of their weighting functions are distributed between the earth's surface and 52 km space. Therefore, using these channels we can sound the vertical distribution and content of ozone. In this section, we describe relaxation iteration and discuss the results of combined inversion.

1. *Relaxation Iteration*

Equation 10 and equation 34 have the same form. For easy reading, we write them as the following

$$\delta I_m = \int_0^\infty K_m(z,\rho)\frac{\delta\rho}{\rho}dz \tag{42}$$

in which the variation weighting function $K_m(z,\rho(z))$ achieve a maximum at the altitude z_{0m}. ρ is $\rho_{O_3}(z)$.

From equation (42), we can obtain the approximate equation as below

$$I_m - \bar{I}_m \approx \int_0^\infty K_m(z,\bar{\rho})\frac{\rho-\bar{\rho}}{\bar{\rho}}dz \tag{43}$$

where ρ and $\bar{\rho}$ are undetermined retrieval and estimation of vertical distribution of ozone, I is the reading value from radiometer in practical remote sensing, but it and $\bar{I}$ represent the radiative intensity calculated from equation (5) and equation (32) using ρ and $\bar{\rho}$ arespectively in our numerical experiments.

Reducing equation (43), we have

$$I_m - \bar{I}_m + \int_0^\infty K_m(z,\bar{\rho})dz \approx \int_0^\infty \frac{K_m(z,\bar{\rho})}{\bar{\rho}}\rho dz$$

Dividing by $\int_0^\infty K_m(z,\bar{\rho})dz$ in the above equation, we obtain

$$\frac{I_m - \bar{I}_m + \int_0^\infty K_m(z,\bar{\rho})dz}{\int_0^\infty K_m(z,\bar{\rho})dz} \approx \frac{\int_0^\infty \frac{K_m(z,\bar{\rho})}{\bar{\rho}}\rho dz}{\int_0^\infty \frac{K_m(z,\bar{\rho})}{\bar{\rho}}\bar{\rho}dz}$$

Acting relaxation principle (Deepak) in the equation above, we have

$$\rho(z_{0m}) = \frac{I_m - \bar{I}_m + \int_0^\infty K_m(z,\bar{\rho})dz}{\int_0^\infty K_m(z,\bar{\rho})dz}\bar{\rho}(z_{0m}) \tag{44}$$

Using equation (44) we can obtain the following practically used iterative formula

$$\rho(z_{0m})^{(n)} = \frac{I_m - I_m^{(n-1)} + \int_0^\infty K_m(z,\rho^{(n-1)})dz}{\int_0^\infty K_m(z,\rho^{(n-1)})dz} \rho(z_{0m})^{(n-1)} \tag{45}$$

where m is the order number of channels ($1 < m < 18$), z_{0m} represents the altitude at which weighting function of channel m approach maximum, n is the times of iteration.

The contraction criterion for this method is

$$\sqrt{\frac{1}{M}\sum_{m=1}^{M}\left(\frac{I_m - I_m^{(n)}}{I_m}\right)^2} \leqslant 1.0\% \tag{46}$$

where M equals 18.

2. *Examples*

Figure 7 to Figure 16 show 10 numerical experiments of remote sensing of ozone vertical distribution. The initial vertical distribution of ozone in all examples is given by standard atmosphere. Solid, dashed and dotted lines in these figures denote the actual, initial guess and inversion profile of ozone respectively.

Figure 7 show a very special example for sounding the ozone profile and content, in which the actual vertical distribution of ozone varies gradually in such a way that its value is 60% larger than its initial value at the earth's surface and increases 2% per km with height.

Figure 8 and Figure 9 show examples of investigation of spatial resolution of the method. In these figures, actual profiles have an increase of 30% relative to the initial value at heights of 35 km to 39 km and 35 km to 44 km respectively.

Figure 10 to Figure 13 show four typical ozone profiles of balloon–sonde (Komhyr et al, 1968), and their initial and inversion profile in spring, summer, fall and winter at Sterling, USA, in which the actual profiles over 35 km are given by us in the way of its increment varying linearly relative to the initial profile with maximum of 44%.

Figure 14 gives the ozone profile of a balloon–sonde and its initial and inversion profiles in Xianghe, near Beijing, China, on August 23, 1985 (Shi et al). The vertical distribution of actual ozone above 33 km is given by the same method as Figure 10.

Figure 15 and Figure 16 show the comparison of results of combined inversion and infrared, and BU inversion only respectively. In Figure 15, dotted line denotes the ozone profile of inversion from BU technique only. In Figure 16, dashed line is both initial and inversion profiles by infrared channels alone.

3. *Discussion*

Several examples are shown in the last section. Table 1 shows the relative errors of density averaged for the altitude; $< E >$, Content; C and the iterative times for Figure 10 to Figure 14. $< E >$ is obtained by the following equation

$$E = \sqrt{\frac{1}{I}\sum_{i=1}^{I}\left(\frac{\rho_i - \rho_i^{(n)}}{\rho_i}\right)^2} \tag{47}$$

where I equals 65. n is 0 for initial guess, and the times of iteration for inversion results.

Table 2 shows the relative errors of ozone density averaged for 12 inversion examples at 10 altitudes; $< I.E. >$. The 12 examples are Figure 7 to Figure 14 and four others which are not shown in this paper. The $< I.E. >$ is obtained from the equation below

$$I.E. = \sqrt{\frac{1}{M}\sum_{i=1}^{M}\left(\frac{\rho_i - \rho_i^{(n)}}{\rho_i}\right)^2}. \tag{48}$$

where $M = 12$ is the numbers of inversion examples used for statistics.

Table 1. Iterative Times and Relative Errors of Ozone Density Averaged for the Altitude; $< E >$ and Content; C for Fig.7–Fig.11

Figure	Iterative Times	Initial Guess (%)		Inversion Results (%)	
		E	C	E	C
Figure 10	5	47.7	1.9	41.8	0.1
Figure11	7	44.6	1.5	25.7	1.1
Figure 12	7	40.2	1.6	22.0	0.5
Figure 13	4	45.9	1.2	24.3	1.1
Figure 14	12	78.6	−27.6	28.2	0.05
Average		51.4	−4.2	28.4	0.6

Table 2. Relative Errors of Ozone Density Averaged for 12 Inversion Examples at 10 Heights; $< I.E. >$

Height (km)	0.0	10.0	15.0	19.0	23.0	26.0	30.0	40.0	50.0	60.0
Initial guess (%)	34.6	55.0	76.1	49.1	24.1	22.0	27.8	40.8	26.4	34.8
Inversion results (%)	38.6*	40.0	21.7	13.9	10.5	5.3	5.6	4.7	6.4	11.9

* This is caused by the inversion error−119.2% at the earth's surface in Figure 14.

1. *Total Content of Atmospheric Ozone*

From Table 1, we find that the relative errors of total content of ozone of inversion results are much less than those of the initial guess. The inversion error is about 1%. Their average values are 0.6. While the error by BU only is more than 1%, and the annual average of errors by infrared technique of Nimbus III alone is 6% (London et al., 1980). Figure 15 and Figure 16 clearly illustrate the reason why our method has greater accuracy.

2. *Ozone Profile*

Figure 10 to Figure 13 show that the ozone profile of inversion is much better than that of initial guess at Sterling, USA in different seasons. They illustrate that it is possible to apply our method at any time at Sterling. Figure 14 shows that the inversion results are still good at Xianghe, China. Figure 10 to Figure 14 illustrate that it is possible to use our method at any time at any place. This conclusion can also be obtained from Table 1 and Table 2. The average errors of the inversion results are much less than those of the initial guess in Table 1. And the inversion results are also better than the initial guess for the relative errors of ozone density averaged for examples in Table 2 except for the earth's surface, which is caused by the inversion error—119.2% at the earth's surface in Figure 14.

As to the precision of inversion results, we find that it depends on the degree of smoothness which the initial profile has relative to the actual profile. The smoother it is, the higher the inversion precision is . And this can be shown clearly in Figure 7 to Figure 14. In Figure 7, the inversion $< E >$ is only 5.7% which is less than any one in Table 1. This is due to the moderate spatial resolution of this method.

Figure 8 and Figure 9 show examples for investigating the spatial resolution of this method. The inversion results in Figure 9 are better than those in Figure 8. Figure 8 indicates that spatial resolution of this method is greater than 4 km. And this is coincident with half-width of weighting function of channel.

Because of the spatial resolution, the undulation of the actual profile cannot be obtained by our method. Therefore the inversion error of Figure 7 is the least in all examples shown for the strong undulation in the lower atmosphere. And Table 2 shows the largest error at the earth's surface, for the same reason as above. But our method still gives the ozone profile of the lower atmosphere shown in Figure 10, Figure 11 etc. The values of inversion errors in Table 1 and Table 2 are still large. These are caused by using the density of 1 km, less than the spatial resolution, in equation (47) and equation (48). Obviously these errors can be decreased if using a density of more than 4 km.

Figure 15 and Figure 16 show that the our method is better than BU and infrared methods only. From Figure 15, we find the actual ozone profile below 15 km cannot be obtained by the BU only. This is the same as Aruga's conclusion. The ozone between 28 km and 38 km is not obtained by infrared method only in Figure 16.

3. *Relaxation Method*

Figure 7 to Figure 14 show that the relaxation described in Section 4.1 is an efficient method. From these Figures and Table 1, we find that the larger the difference between initial and actual profiles and the stronger the undulation of actual profile, the greater the number of iterations required.

V. CONCLUSION AND PROBLEM

Knowing the temperature profile of the atmosphere and using a narrow width of infrared channels in ozone 9.6 μm absorption band, we can overcome the difficulty of sounding the ozone profile below the profile main-peak. The width of these channels is 0.01 cm^{-1}, less than the Lorentz half-width of ozone absorption at the earth's surface, which method may be applied to remote sounding of other constituents of the atmosphere. Using combined satellite BU and satellite and ground infrared channels, we can obtain satisfactory precision in determining ozone content, just about 1%, and vertical distribution from the earth's surface to 65 km space. Numerical experiments show that the relaxation described in this paper is an efficient inversion method. Some semi-analysis functions for calculating backscattered ultraviolet also save a lot of computer time in this paper.

The problem is that this kind of infrared radiometer cannot be produced at present. Therefore it is necessary for engineers to put some effort into designing this kind of radiometer.

REFERENCES

Aruga, T. and Lgarashi, T., (1976), Vertical Distribution of Ozone: A new method of determination using satellite measurement, *Applied Optics*, **15**(1): 261–272.

Bojkov, J.,R.D., Mateer, C.L. (1980), Report of the Meeting of Experts on Assessment of Performance Characteristics of Various Ozone Observing Systems, Boulder, July 1980, WMO GLOBE OZONE RESEARCH AND MONITORING PROJECT REPORT, No.9.

Cheng Minghu, (1985), Remote Sensing of Vertical Distribution and Total Content of Atmospheric Ozone, Master Thesis, Institute of Atmospheric Physics, Academia Sinica (in Chinese).

Deepak, Adarsh, *Inversion Methods*, 67–111.

Heath, Donald F., Mateer, Carlton L., and Krueger, Arlin J., (19/3), The Nimbus–4 Backscatter Ultraviolet (BUV) Atmospheric Ozone Experiment–Two Years' Operation, *Pure and Applied Geophysics* (PAGEOPH) Vol.106–108 (1973 / V–VII) 1238–1253.

Heath, Donald F., Krueger Arlin J., and Park, H., (1978), Nimbus 7 User's Guide, C.R. Madnicol ed, NASA Goddard Space Flight Center, 175–211, August 1978.

Houghton, J.T., Taylor, F.W., Rodgers, C.D., (1984), Remote Sounding of Atmospheres, Cambridge University Press.

Komhyr, W.D., Grass, R.D., Proulx, R.A., (1968), Ozonesonde Intercomparison Tests, ESSA Techn. Rep. ERL85–APCL4.

Liou, Kuo–Nan, (1980), An Introduction to Atmospheric Radiation, Academic Press, New York.

London, Julius and Angell, James K., *Stratospheric Ozone and Man;* Volume I, Chapter 1, The Observed Distribution of Ozone and Its Variation.

McClatchey, R.A. et al, (1972), *Optical Property of the Atmosphere* (3rd ed.) AFCRL–72–0497.

McClatchey R.A. et al, (1973), AFCRL Atmospheric Absorption Line Parameters Compilation, AFCRL–TR–73–0096, 26 Jan., 1973.

Prabhukara, C., Courath, B.J., Hanel, R.A. and Williamson, E.J., (1970), Remote Sensing of Atmospheric Ozone Using the 9.6 μm Band, *J. Atmos. Sci.*, **27**: 689.

Randeyger, A.K., On the Determination of the Atmospheric Ozone Profile for Ground Based Microwave Measurements, *Pure and Applied Geophysics*, **118**(5): 1052–1065.

Sekihara, K. and Walshaw, C.D. (1969), *Ann. Geophys.* **25**: 233–241.

Shafin, Yu. A., (1970), *Isv. Atm. Ocean. Phys.* **6**: 696–703.

Shi Guangyu et al, Balloon Sounding of Ozone and Aerosol Profile of 0–33 km (in press).

Zeng Qingcun, (1974), *Principle of Atmospheric Infrared Remote Sensing*, Science Press, Beijing, (in Chinese).

Zhou Xiuji et al, (1982), *Principle of Atmospheric Micrometer Radiation and Remote Sensing*, Science Press, Beijing (in Chinese).

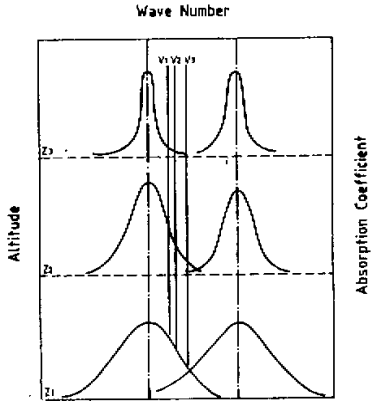

Fig.1. Determination of channel wave number.

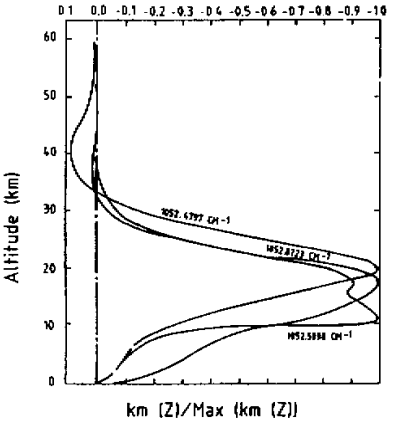

Fig.2. Variation weighting function of satellite infrared narrow channel.

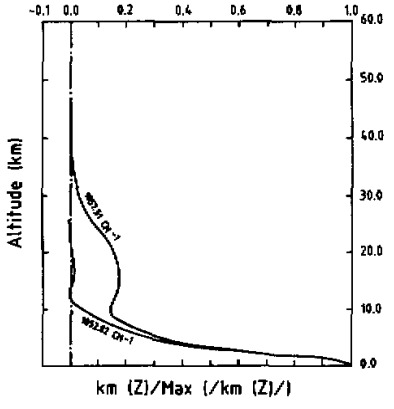

Fig.3. Variation weighting function of ground based narrow channels.

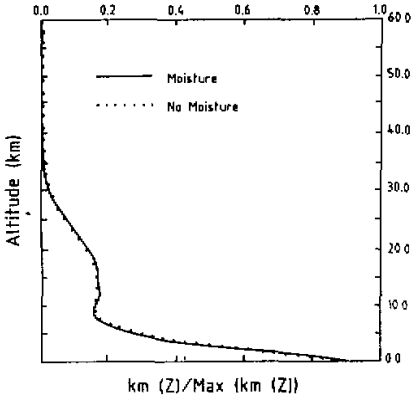

Fig.4. Variation weighting function with and without the effect of moisture.

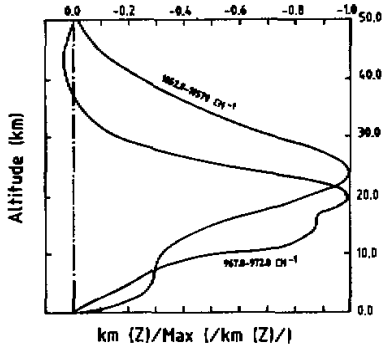

Fig.5. Variation weighting function of satellite infrared wide channel.

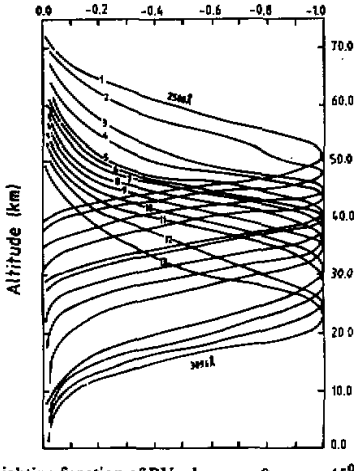

Fig.6. Weighting function of BU where $\varphi = 0$, $\varphi_0 = 45^0$, $\theta = \theta_0 = 30^*$.

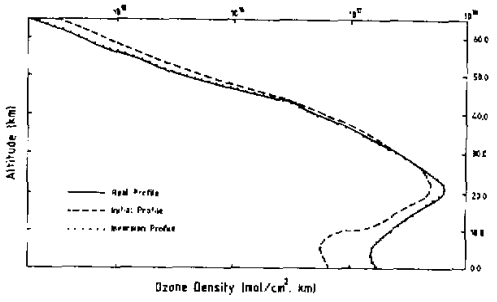

Fig.7

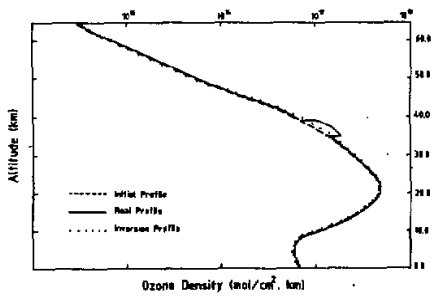

Fig.8

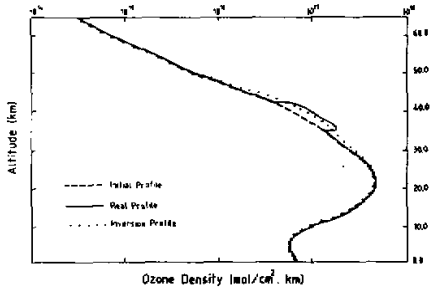

Fig.9

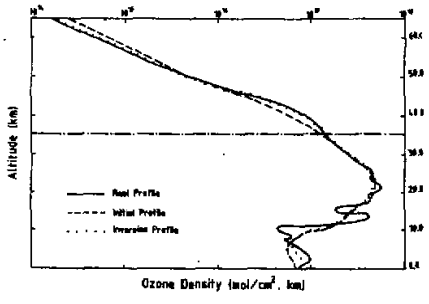

Fig.10

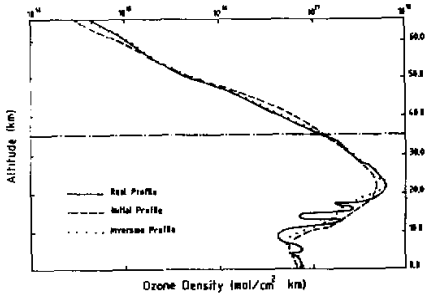

Fig.11

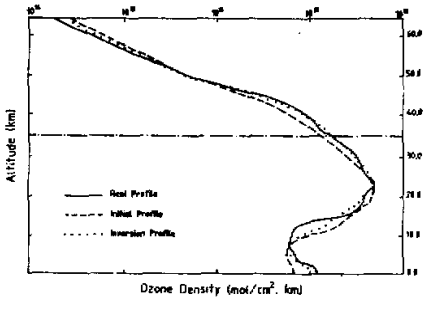

Fig.12

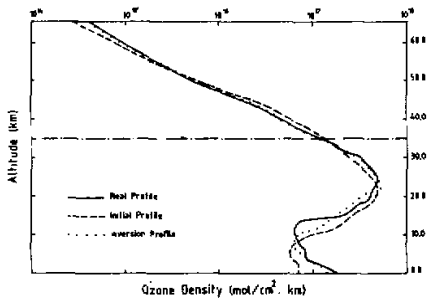

Fig.13

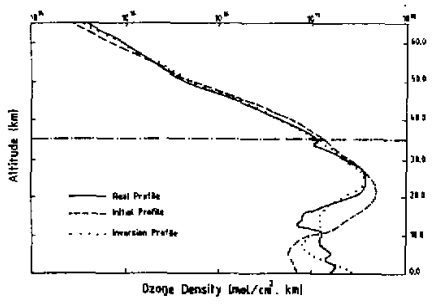

Fig.14

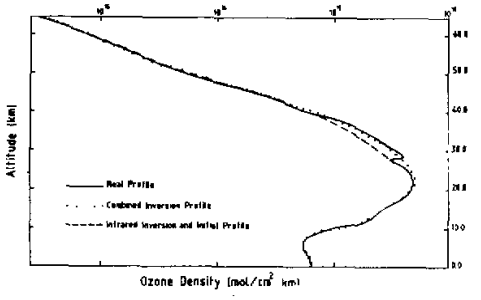

Fig.15. Comparison of results of combined and infrared inversion.

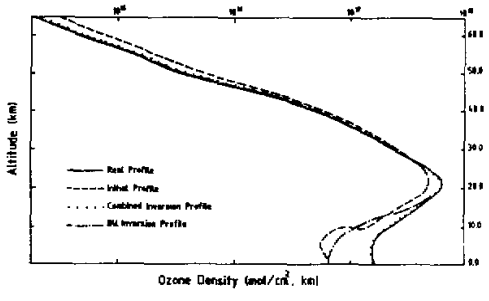

Fig.16. Comparison of results of combined inversion and BU inversion.